The International Journal of Advanced Manufacturing Technology (2021) 116:3507–3515
https://doi.org/10.1007/s00170-021-07579-1

ORIGINAL ARTICLE

Design of a spatial constant-force end-effector for polishing/deburring operations

Bingxiao Ding[1] · **Jiyu Zhao**[1] · **Yangmin Li**[2]

Received: 27 April 2021 / Accepted: 26 June 2021 / Published online: 21 July 2021

Abstract

Controlling the contact force on workpieces is a challenging task for industrial deburring operations. To solve this issue, a novel constant force mechanism (CFM) based on the combination of positive and negative stiffness mechanism is proposed by using folding beam and bi-stable beam mechanisms. Without using any additional sensors and control algorithms, the proposed CFM can produce a travel range in constant force manner. In this paper, the design concepts, analytical model, finite element analysis (FEA) simulation and experimental studies are presented and discussed. Firstly, a novel spatial CFM is proposed and the pseudo rigid body (PRB) method is used to establish the mathematical model of the whole mechanism. Then, the FEA simulation is performed to validate the correctness of theoretical analysis. In addition, to eliminate the force variation, particle swarm optimization (PSO) method is utilized to find optimal architectural parameters solutions of the CFM. Finally, the experimental tests are performed to verify the performance of the designed CFM. The configuration design and parameter optimization proposed in this paper can be further applied to the design of other types of CFM mechanisms for polishing operations as well.

Keywords Compliant mechanism · Constant force mechanism · Polishing/deburring operation

Nomenclature

Abbreviations

CFM	Constant force mechanism
FEA	Finite element analysis
PRB	Pseudo rigid body
PSO	Particle swarm optimization
VCM	Voice coil motor

Subscripts

b	Related to the bistable beam mechanism
p	Related to the folding beam mechanism

Variables

θ	Inclination angle
L	Length of a beam

✉ Jiyu Zhao
zjy13575154725@hotmail.com

✉ Yangmin Li
yangmin.li@polyu.edu.hk

[1] School of Physics and Electromechanical Engineering, Jishou University, 416000, Jishou, Hunan China

[2] Department of Industrial and Systems Engineering, The Hong Kong Polytechnic University, 999077 Hung Hom, Hong Kong SAR China

1 Introduction

Robots are increasingly adopted for workpieces deburring and polishing to overcome the problems of low production efficiency, high cost and poor consistency in manual polishing [1–3]. As pointed out in previous research, the contact force between the grinding tool and workpiece is the key factor that affects the polishing quality [4–6]. Excessive or insufficient contact force would greatly impair the quality of the surface roughness. Thus, it becomes an urgent issue to maintain the constant contact force in the grinding process to ensure the polishing quality and consistency [7–9].

Generally speaking, the constant force can be realized by two methods [10]. The first way is an active compliance force control. The polishing force can be controlled by a closed-loop controller. In addition, the robot can actively adapt to the changing of the machined surface to ensure the constant contact force [11, 12]. For instance, Masoud et al. proposed a resultant force control strategy for light abrasive surface grinding. The performance of resultant force control strategy with real-time tool deflection compensation algorithm is validated by the grinding experimental studies [13]. Wang et al. designed a vibration suppression method for large thin-walled shell grinding

based on force control algorithm. The experimental results show that the grinding depth error is less than ±0.1 mm, and the polishing quality of the workpiece surface can be significantly improved [14]. Xie proposed a method for grinding blade free-form surface based on PSO algorithm. The impedance controller based on PSO algorithm can realize the function of impedance parameters adjustment and the contact force between workpiece and grinding tool can be accurately controlled [15]. Xu put forward a zero drift and gravity compensation algorithm for robot belt grinding with complex geometry which combines force-position hybrid control strategy with PI controller to maintain the stability of force control during robot grinding process [16]. Although constant contact force can be realized by aforementioned methods, needing complex controller algorithm and expensive sensors limits their further applications. Moreover, the positioning accuracy would degrade the force control performance through the force-position hybrid control method which was used to realize active compliance force control [17].

In contrast, another method is the passive compliance force control which uses rigidity of the robot and the flexibility of the force controllable end-effector to realize force control. The path planning is realized by the robotic arm and the control of force is realized by the end-effector respectively [18, 19]. Mohammad proposed a force controllable end-effector for automatic deburring, which can reduce the inertial effect of polishing motor and spindle driven by micro driver [20]. Chen proposed an end-effector, including gravity compensation force controller and two new eddy current dampers, which were integrated into the end-effector to improve the dynamic performance of the system and suppress the vibration during grinding and polishing [21]. Liu proposed a polishing mechanism with characteristics of simple structure, small mass and good compliance performance. In addition, hardware circuit construction and force control algorithm design are modeled and analyzed detailedly [22]. Tang proposed a multi degree of freedom flexible terminal actuator for mould polishing robot. The buffer spring ensures the working pressure between the grinding head and the workpiece changes in a constant range [23]. The key component of the force controllable end-effector is the constant force compensation device. At present, the commonly used constant force compensation devices are type of electromagnetic, air bag and linear motor [24].

However, the above constant force compensation devices possess the disadvantages of low precision, slow response and poor environmental adaptability. In view of these shortcomings, a novel spatial CFM for grinding operation based on distributed flexure beam is proposed in this paper. The remainder of this paper is organized as follows: the design concepts of proposed CFM is depicted in Section 2; Section 3 establishes the mathematical model of the whole CFM and obtains the relationship between output force and input displacement; ANSYS Workbench is utilized to verify correctness of the theoretical analysis in Section 4; To eliminate the force variation, the PSO method is adopted to optimize the CFM in Section 5; In addition, experimental studies are conducted in Section 6 to verify the performance of the CFM; Finally, conclusions are made in Section 7.

2 Design concepts

CFM is a passive constant force system, which can provide a constant output force within a certain range of deformation relying on the characteristics of the structure itself. Compared with the active constant force system, the CFM can reduce the use of expensive sensors and complex control algorithms, thus reducing the cost.

To realize a certain constant force output, the combination of positive stiffness mechanism with negative stiffness mechanism is a typical method. Generally, the straight beam is taken as positive stiffness mechanism to neutralize negative stiffness region of bi-stable beam mechanism. However, the traditional symmetrical straight beam mechanism cannot take full advantage of negative stiffness region of the bi-stable beam mechanism. To overcome this issue, a novel type of folding beam as a positive stiffness mechanism is designed for the purpose of increasing the constant force travel range. The force-displacement relationship comparison of designed positive stiffness mechanism and straight beam mechanism is depicted in Fig. 1, which shows that the folding beam mechanism has a good linearity in long range.

The autonomous polishing scenario using CFM system is shown in Fig. 2, the end-effector including voice coil motor (VCM), CFM and grinding head are installed at the end of robot arm through the connecting flange. When the VCM works, it drives the grinding head to approach the workpiece. As an intermediate part, the CFM placed between the motor unit and grinding tool which mounted on the CFM. Due to the constant force output characteristics of the CFM, the constant force can be maintained between grinding head and the workpiece in a certain range of motion, so as to finish the precision grinding and polishing operations.

3 Analytical model of designed CFM

In this part, the analytical model of bi-stable beam and folding beam is established respectively. Then, the relationship between input force and output displacement of the CFM is derived. As shown in Fig. 2, the CFM is composed of three branched chains and a central column,

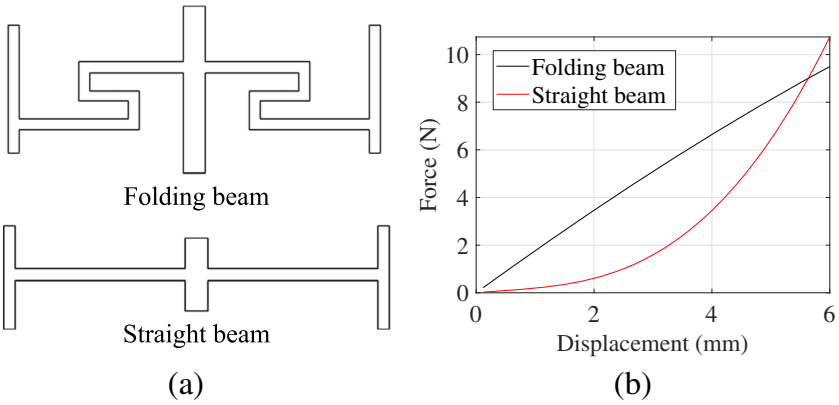

Fig. 1 Comparison of two kinds of positive stiffness mechanism. (**a**) CAD model. (**b**) Force-displacement curve comparison

each chain composed of a parallel bi-stable beams and a folding beam mechanism. Considering the identical architecture of each branch, an arbitrary chain is selected for analysis.

3.1 Modeling of bi-stable beam

As shown in Fig. 3, buckling and deformation of the bistable beam is resulted by the loading force F_n. In this figure, L denotes the length of the beam, θ represents the inclination angle between the bi-stable beam and the X axis, and Δx_b is the displacement of the bistable beam under the force of F_n along Y direction. When the force F_n loading on the bistable beam exceeds the critical force of the material, the buckling force of the i_{th} critical point of the guide beam can be obtained referring to the previous studies [25, 26]:

$$F_n = \frac{4EI(\lambda_n)^2}{L^2} \tag{1}$$

where $\lambda_n = \pi, 4.493, 2\pi, ...,n = 1, 2, 3, ...$

Therefore, the negative stiffness of bistable beam k_b can be expressed as follow:

$$k_b \approx \frac{33EI}{L^3} \tag{2}$$

where E represents the elastic modulus of the material, $I = bd^3/12$ is the inertia moment of the guide beam, d is the thickness of the beam, and b is the width of the beam. Referring to Eqs. (1) and (2), the force-displacement relationship of the bistable beam can be written as:

$$F_n = ES\frac{\Delta x_b}{L}\left(\frac{\Delta x_b}{L} - \sin\theta\right)\left(\frac{\Delta x_b}{L} - 2\sin\theta\right) \tag{3}$$

where $S = b \cdot d$ is the cross sectional area of the guide beam.

3.2 Modeling of folding beam

The deformation of the folding beam is shown in Fig. 4, in which L_{s1}, L_{s3} and L_{s5} represent the length of each beam respectively, and Δx_f is the displacement of the

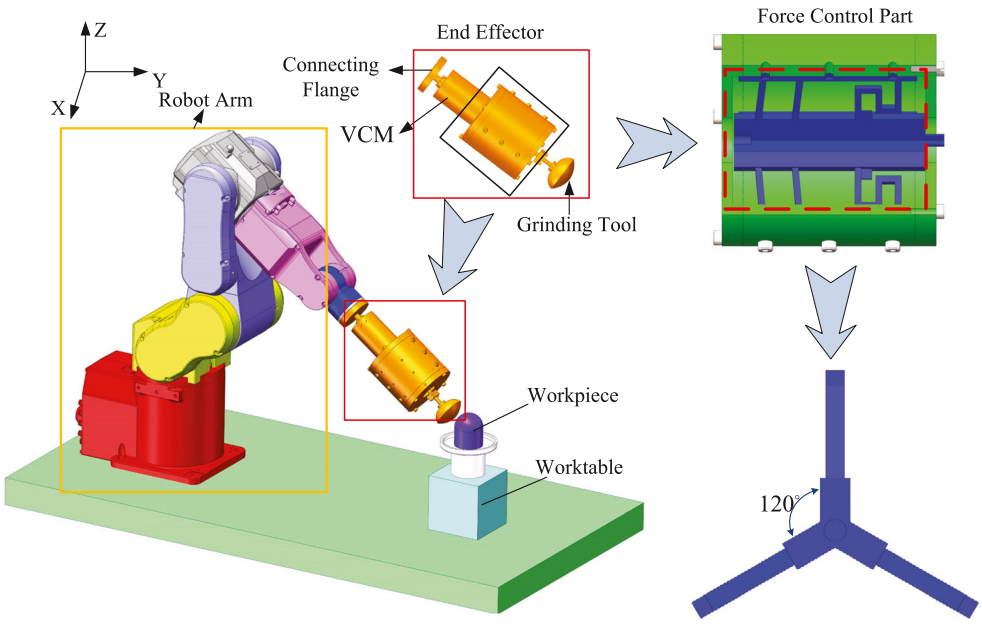

Fig. 2 The autonomous polishing scenario using CFM end-effector

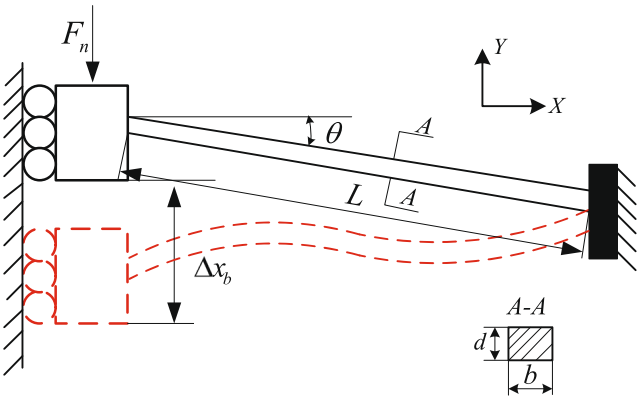

Fig. 3 Buckling deformation of bi-stable beam mechanism

folding beam due to the external force F_p. The folding beam mechanism can be decomposed of three cantilevers ab, cd and ef, and the deformation of each cantilever is $\Delta x_{L_{s1}}$, $\Delta x_{L_{s3}}$ and $\Delta x_{L_{s5}}$ respectively. According to the superposition principle, the total deformation Δx_f of the folding beam mechanism and stiffness k_f of mechanism can be derived as following [27]:

$$\Delta x_f = \Delta x_{L_{s1}} + \Delta x_{L_{s3}} + \Delta x_{L_{s5}} \tag{4}$$

$$\frac{1}{k_f} = \frac{1}{k_{ab}} + \frac{1}{k_{cd}} + \frac{1}{k_{ef}} \tag{5}$$

ab, cd and ef beams can be regarded as semi-fixed beam model under a concentrated load force $2F_p$, as shown in Fig. 5. In Fig. 5a, the length of the fixed beam is $2L_{si}$, and the middle of the beam is subjected to a downward concentrated load $2F_p$. Under the force of $2F_p$, the maximum deformation of the beam is δ_{max}. If the fixed beam is spilt in the middle, a semi-fixed beam can be obtained as shown in Fig. 5b. The bending moment of the semi-fixed beam at the fixed end is:

$$M_o = \frac{F_p L_{si}}{2} \tag{6}$$

The shear force is:

$$R_s = F_p \tag{7}$$

The axial force can be neglected because it is too small compared with shear force and bending moment.

In a semi-fixed beam, the maximum displacement δ_{max} is composed of the displacement δ_{M0} caused by the bending moment M_0 and the displacement δ_s caused by the shear force R_s. Therefore, the following equation can be obtained:

$$\delta_{max} = \delta_{M_0} + \delta_s \tag{8}$$

According to Hooke's Law:

$$\frac{1}{k_{max}} = \frac{1}{k_{M_0}} + \frac{1}{k_s} \tag{9}$$

For a semi-fixed beam, because of bending moment the maximum deflection occurs in the middle of the beam:

$$\delta_{M_0} = \frac{F_p L_{si}^3}{12EI} \tag{10}$$

Therefore, the stiffness caused by the bending moment of the fixed beam can be expressed as:

$$k_{M_0} = \frac{12EI}{L_{si}^3} \tag{11}$$

where L_{si} is the length of the semi-fixed beam. For semi-fixed beams, the stiffness constant caused by bending moment is half of that of fixed beams. For semi-fixed beams, the maximum deflection due to shear force is:

$$\delta_s = \frac{6F_s L_{si}}{5AG} \tag{12}$$

where G is the shear modulus, $G = E/2(1+\mu)$, μ is the Poisson's ratio, and A is the cross section area of the beam.

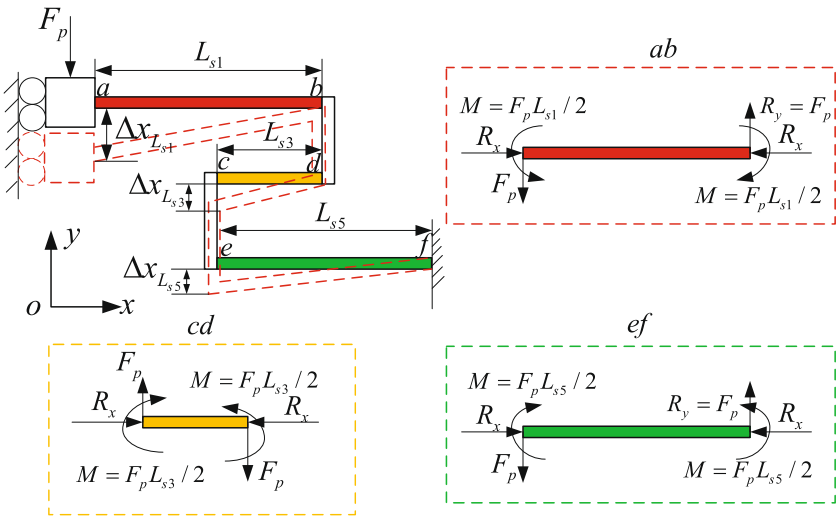

Fig. 4 Components of folding beam

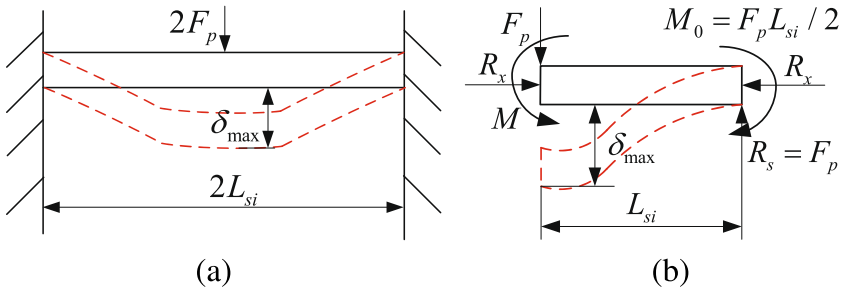

Fig. 5 Beam analysis. (**a**) Fixed-fixed beam under transverse loading. (**b**) The model of semi-fixed beam

According to known conditions, $F_s = F_p/2$, the results are as follows:

$$\delta_s = \frac{6}{5}\frac{(1+\mu)F_s L_{si}}{AE} \tag{13}$$

The stiffness is:

$$k_s = \frac{5}{6}\frac{AE}{(1+\mu)L_{si}} \tag{14}$$

By adding the above formula into (5), we can get the following results:

$$\frac{1}{k_f} = \frac{L_{s1}^3 + L_{s3}^3 + L_{s5}^3}{12EI} + \frac{6(L_{s1}+L_{s3}+L_{s5}) + 6\mu(L_{s1}+L_{s3}+L_{s5})}{5EA} \tag{15}$$

The relationship between the output force F_p and the input displacement Δx_f of the folded beam can be obtained by combining the above formula.

$$F_p = k_f \Delta x_f \tag{16}$$

When a branch chain of the CFM is subjected to an external force, the deformation of the bistable beam equals to the deformation of the folded beam, namely $\Delta x_b = \Delta x_f$. By adding the above formula into (3) and (16), the relationship between the force of a branch chain F_1 and the input displacement Δx can be obtained:

$$\begin{aligned} F_1 &= F_n + F_p \\ &= ES\frac{\Delta x}{L}\left(\frac{\Delta x}{L} - \sin\theta\right)\left(\frac{\Delta x}{L} - 2\sin\theta\right) + \left(\frac{L_{s1}^3 + L_{s3}^3 + L_{s5}^3}{12EI} + \frac{6(L_{s1}+L_{s3}+L_{s5}) + 6\mu(L_{s1}+L_{s3}+L_{s5})}{5EA}\right)^{-1}\Delta_x \end{aligned} \tag{17}$$

4 FEA verification

In this section, the FEA simulation is utilized to verify the correctness of the theoretical analysis. The adopted material is PLA-ST. The material properties are with Young modulus 1477 MPa, Poisson's ratio 0.3, and the density 1.25 g/cm^3. The original dimensional parameters of the designed CFM are listed in Table 1.

The ANSYS Workbench is adopted to verify the performance of bistable and folding beams and the simulation results are depicted in Fig. 6. Referring to the Fig. 6a, the critical buckling force occurs at point of (1.3, 8.46) in theoretical which very closes to the point of (1.2, 9.99) in FEA results. At the same point in folding beam mechanism, the force value 2.86 N is also closed to the 3.09 N. In addition, the slope of both negative stiffness and positive stiffness in theoretical and FEA simulation are very consistent. Referring to Fig. 7, it can be concluded that theoretical and simulation results are both present constant force characteristic and the trends of the two curves are closely within the region of 1.3–5.28 mm. The differences between the theoretical and FEA results are acceptable because of the established mathematic model ignores the effects of intermediate beams. However, the flatness of constant force travel range is poor, which is not suitable for the application requirements. Therefore, it is necessary to optimize architecture parameters to eliminate/reduce the force variation in the specified constant force range.

5 Parameter optimization

The performance and dimensional size of the CFM is affected by the designed architecture parameters. For example, the parameter of inclination angle, length, and width of the CFM plays an important influence on the constant force travel range. The design goal of CFM is

Table 1 Original architecture parameters of the CFM

Parameter	Value	Unit
L	30	mm
b	1.0	mm
d	10	mm
θ	5.0	deg
L_{s1}	18	mm
L_{s3}	5	mm
L_{s5}	18	mm

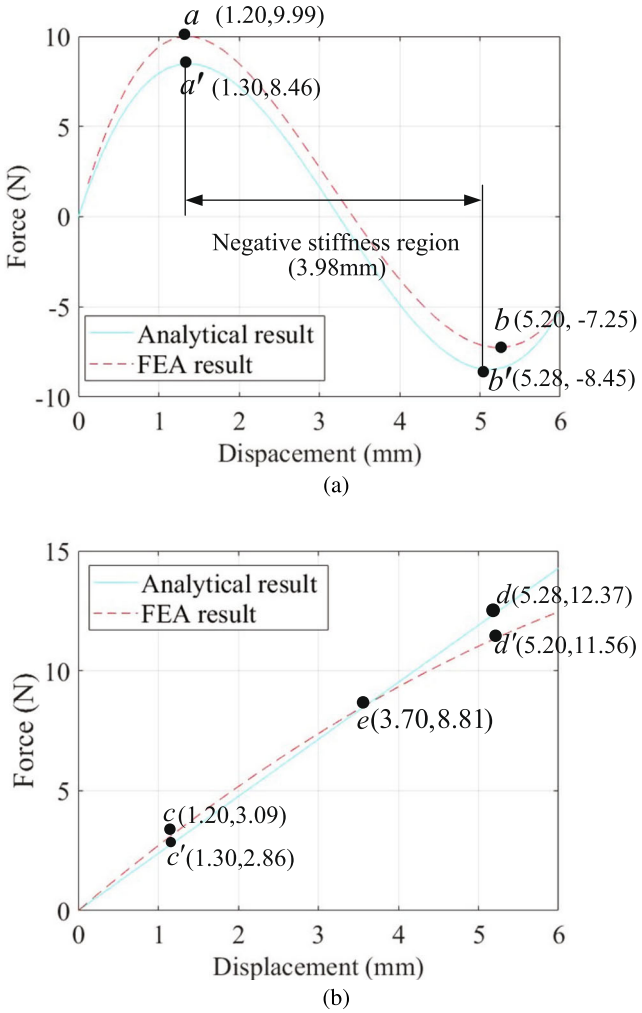

Fig. 6 FEA verification. (**a**) Theoretical and FEA results comparison of bistable mechanism. (**b**) Theoretical and FEA results comparison of folding beam mechanism

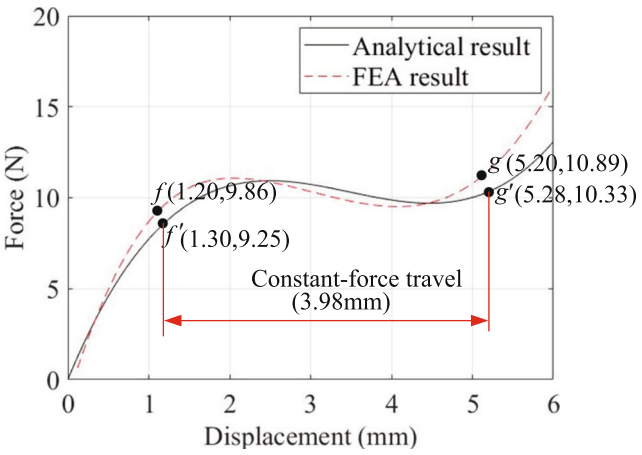

Fig. 7 Theoretical and FEA results comparison of the designed CFM

taken as an end-effector which mounted at the end of robotic arm to implement polishing operation. Hence, the size compactness and mass of the CFM need to taken into consideration in terms of robotic loading capacity. In addition, considering the manufacturing method in this research, the width d of the flexure beam is not less than 1 mm. Because of the structural limitation, the length of L is no longer than 40 mm. The bigger inclination angle of the bistable beam, the larger negative stiffness displacement can be generate, but the larger driving force required to generate buckling. To reduce the manufacturing error, the inclination angle should be larger than 4°. To eliminate force variation, the aforementioned design objectives and constraint conditions are summarized as follows:

$$Objective: min\sigma = \sqrt{\frac{1}{N}\sum_{1}^{N}(F_x - \mu)^2} \tag{18}$$

$$Subject\ to = \begin{cases} 15 \le L_{s1} \le 20, \\ 2 \le L_{s3} \le 5, \\ 15 \le L_{s5} \le 20, \\ 1 \le b \le 3, \\ 1 \le d \le 15, \\ 20 \le L \le 40, \\ 4° \le \theta \le 7°, \end{cases} \tag{19}$$

where σ is the mean square error, F_x represents the force value extracted in a given interval, and μ is the average force value of selected region. When the value of σ is small or becomes zero, it means that force variation is reduced and eliminated.

Taking all the issues into account, PSO method is adopted to find the optimal solution of each parameter. In this research, the 200 sampled points are randomly selected in the range of 2.5 to 4.5 mm. The obtained optimal parameters are listed in Table 2. Substituting the optimal architecture parameters into the analytical model of CFM and conducting the simulation analysis, the FEA results are very consistent with analytical results as shown in Fig. 8. It is further validated the correctness of the theoretical analysis. Referring to the Fig. 8, the line located in the region of 2.5 to 4.5 mm is approximately a horizontal line,

Table 2 Optimized architecture parameters of the CFM

Parameter	Value	Unit
L	35.0	mm
b	2.0	mm
d	4.0	mm
θ	5.1	deg
L_{s1}	20.0	mm
L_{s3}	4.0	mm
L_{s5}	19.0	mm

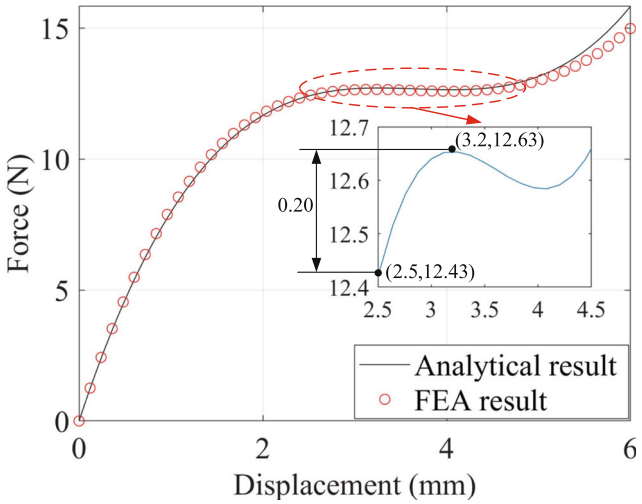

Fig. 8 Comparison of FEA simulation results and optimized results of the CFM

in which the maximum value is 12.63 N, the minimum value is 12.43 N and the flatness is 98.41%.

6 Experimental verification

To test the performance of the proposed CFM, the prototype is fabricated and a series of experimental studies are performed in this section.

6.1 CFM fabrication

To validate the proposed design, the experimental system is built as depicted in Fig. 9, including the designed CFM (fabricated by 3D printing), VCM, grating ruler, force sensor, motor driver, and industrial control computer. To isolation the external disturbances from the environment, the whole experimental system is installed on an anti-vibration optical table. The commercial linear servo amplifier (model: ACJ-055-18) is adopted to drive the VCM (model: TMEC100-015-000) with a nominal travel range of 5 mm. A grating ruler (model: LaRW1-3D, Fagor Automation) is utilized to measure the displacement of the CFM. A force sensor (DS2-XD) with a range of 50 N and a resolution of 0.01 N is chosen to measure the reaction force.

6.2 Relationship test between force and displacement

During the experimental study, the actuating force and output displacement of the CFM are measured by the force sensor and grating ruler respectively. The comparison of FEA, theoretical calculation and experimental results is shown in Fig. 10. Referring to the experimental results, the constant force range of the CFM starts from 2.68 to 4.81 mm with the constant force is 11.92 N. Compared with the results of finite element analysis and theoretical calculation, the range of constant force increases by 0.18 mm, while the magnitude of constant force decreases by 0.68 N.

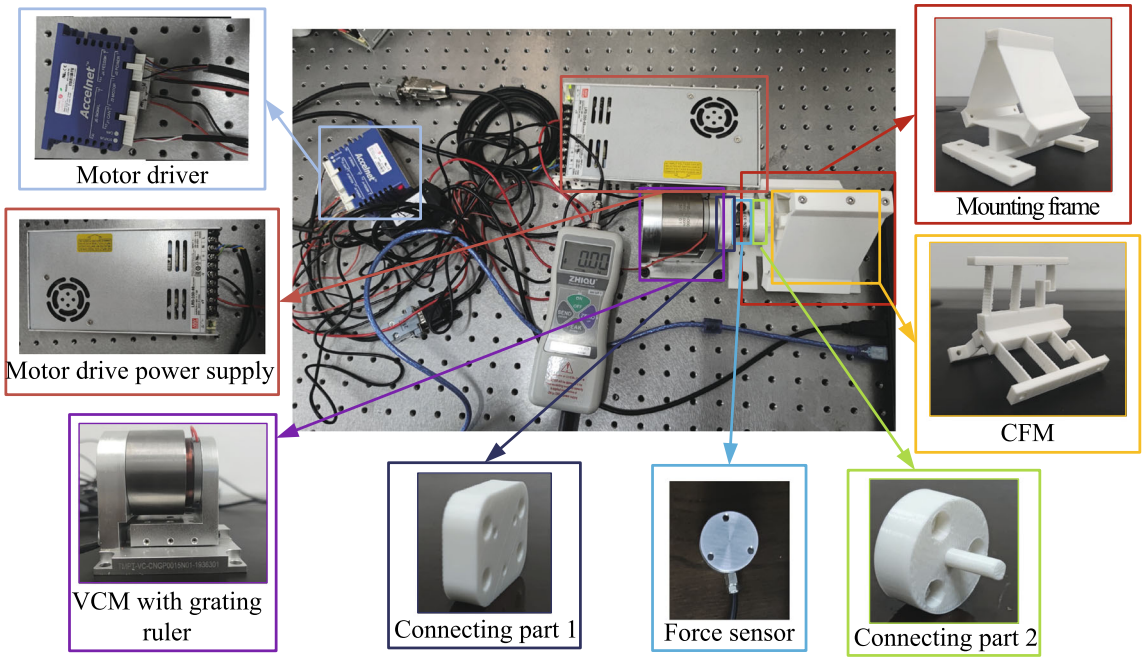

Fig. 9 Experimental system

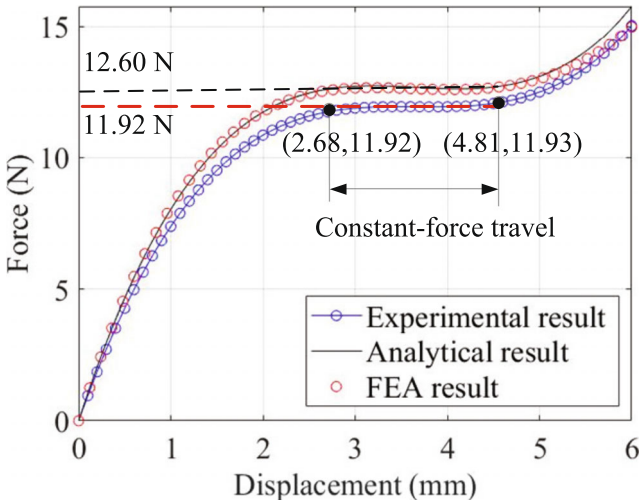

Fig. 10 Experimental results comparison with FEA simulation and analytical results

7 Conclusions

This paper presents the design, modeling, simulation, optimization and experimental studies of a spatial CFM for potentially applications in polishing operations. In order to enhance the mechanism stiffness and structure compactness, a parallel spatial CFM based on positive stiffness mechanism and negative stiffness mechanism is designed. To make full use of negative stiffness region, a novel folding beam mechanism with good linearity is designed and the force displacement relationship model referring to the PRB method is established. In addition, to eliminate the force variation, the PSO method is utilized to optimize the architectural parameters. According to the comparison of FEA results of optimized architecture and original design, the flatness in constant travel range is highly improved. Experimental results show that the proposed designed CFM possesses a good characteristic of output constant force. In our future works, multi-body dynamics method will be used to the CFM to better understand its dynamic performance.

Author contribution Bingxiao Ding wrote this paper and revised designed mechanism. Jiyu Zhao designed mechanism and conducted experimental verification. Bingxiao Ding and Yangmin Li revised this paper.

Funding This work is supported by the Huxiang High Level Talent Project of Hunan Province (Grant No. 2019RS1066), the Education Department of Hunan Province (Grant No. 19C1520), the National Natural Science Foundation of China (Grant No. 51575544), and the General Research Fund of the Research Grants Council(RGC) of Hong Kong, China (Grant No. PolyU 152137/19E).

Availability of data and material The data of this study are available from the first author or corresponding author upon reasonable request.

Declarations

Conflict of interest The authors declare no competing interests.

References

1. Wan S, Zhang X, Wang W et al (2019) Effect of pad wear on tool influence function in robotic polishing of large optics. Int J Adv Manuf Technol 102:2521–2530
2. Tao B, Zhao X, Ding H (2019) Mobile-robotic machining for large complex components: a review study. Sci China-Technol Sci 62(8):1388–1400
3. Mohammad AEK, Wang D (2015) A novel mechatronics design of an electrochemical mechanical end-effector for robotic-based surface polishing. In: IEEE/SICE int symposium on sys integration (SII), pp 127–133
4. Domroes F, Krewet C, Kuhlenkoetter B (2013) Application and analysis of force control strategies to deburring and grinding. Mod Mecha Eng 3(2A):11–18
5. Zhu DH, Xu XH, Yang ZY et al (2018) Analysis and assessment of robotic belt grinding mechanisms by force modeling and force control experiments. Tribol Int 120:93–98
6. Khaghani A, Cheng K (2020) Investigation on multi-body dynamics based approach to the toolpath generation for ultraprecision machining of freeform surfaces. Proc Institut Mecha Eng Part B J Eng Manuf 234(3):571–583
7. Kim U, Lee DH, Kim YB et al (2017) A novel 6-axis force/torque sensor for robotic applications. IEEE/ASME Trans Mechatron 22(3):1381–91
8. Budak E (2000) Improving productivity and part quality in milling of litanium based impellers by chatter suppression and force control. Ann ClRP 49(1):31–36
9. Tian F, Li Z, Lv C et al (2016) Polishing pressure investigations of robot automatic polishing on curved surfaces. Int J Adv Manuf Technol 87:639–646
10. Lopes A, Almeida F (2008) A force-impedance controlled industrial robot using an active robotic auxiliary device. Robot Comput Integr Manuf 24:299–309
11. Solanes JE, Gracia L, Benavent PM et al (2018) Adaptive robust control and admittance control for contact-driven robotic surface conditioning. Robot Comput Integr Manuf 54:115–132
12. Xian JS, Xi Z et al (2018) Fuzzy adaptive hybrid impedance control for mirror milling system. Mechatron 53:20–27
13. Latifinavid M, Donder A, Konukseven EI (2018) High-performance parallel hexapod-robotic light abrasive grinding using real-time tool deflection compensation and constant resultant force control. Int J Adv Manuf Technol 96(9-12):3403–3416
14. Wang QL, Wang W, Zheng YL et al (2021) Force control-based vibration suppression in robotic grinding of large thin-wall shells. Robot Comput Integr Manuf 67:1–12
15. Xie QL, Zhao H, Wang T et al (2019) Adaptive impedance control for robotic polishing with an intelligent digital compliant grinder. Int Conf Intel Rob App pp 482–484
16. Xu XH, Zhu DH, Zhang HY et al (2019) Application of novel force control strategies to enhance robotic abrasive belt grinding quality of aero-engine blades. Chin J Aeronaut 32(10):2368–2382
17. Du H, Sun Y, Feng D et al (2015) Automatic robotic polishing on titanium alloy parts with compliant force/position control. Proc Instit Mech Eng Part B J Eng Manuf 7:1180–1192
18. Liao L, Xi FF, Liu KF (2008) Modeling and control of automated polishing/deburring process using a dual-purpose compliant toolhead. Int J Mach Tools Manuf 48(12-13):1454–1463

19. Satake U, Enomoto T, Obayashi Y et al (2018) Reducing edge roll-off during polishing of substrates. Prec Eng 51:97–102
20. Mohammad AEK, Hong J, Wang DW et al (2018) Design of a force-controlled end-effector with low-inertia effect for robotic polishing using macro-mini robot approach. Robot Comput Integr Manuf 49:54–65
21. Chen F, Zhao H, Li DW et al (2019) Contact force control and vibration suppression in robotic polishing with a smart end effector. Robot Comput Integr Manuf 57:391–403
22. Liu X, Zhang T, Li J et al (2018) A novel end-effector for robotic compliant polishing. IEEE Int Conf Rob Biomime pp 1858–1863
23. Tang J, Wang T, Yan ZQ et al (2016) Design and analysis of the end-effector of the flexible polishing robot. Key Eng Mater 693:58–63
24. Chaoui MD, Leonard F, Abba G et al (2019) Improving surface roughness in robotic grinding process, ROMANSY 22, Robot Design, Dynamics and Control. Springer, New York, pp 363–369
25. Holst GL, Teichert GH, Jensen BD (2011) Modeling and experiments of buckling modes and deflection of fixed-guided beams in compliant mechanisms. J Mechan Des 133:051002-1
26. Zhao J, Jia JY, He XB et al (2008) Post-buckling and snap-through behavior of inclined slender beams. J Appl Mechan 75:041020-1
27. Chi WW, Azid AA, Majlis BY (2010) Formulation of stiffness constant and effective mass for a folded beam. Arch of Mechan 62(5):405–418